Journal of Materials Chemistry A

Accepted Manuscript

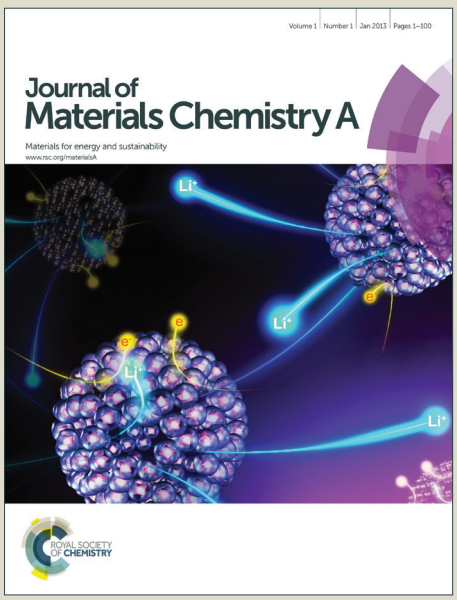

ROYAL SOCIETY OF CHEMISTRY

www.rsc.org/materialsA

Cite this: DOI: 10.1039/c0xx00000x

www.rsc.org/xxxxxx

ARTICLE TYPE

Black TiO_2 Nanotube Arrays for High-Efficiency Photoelectrochemical Water-Splitting

Houlei Cui,[a] Wei Zhao,[a] Chongyin Yang,[a] Hao Yin,[a] Tianquan Lin,[a] Yufeng Shan,[a] Yian Xie,[a] Hui Gu,[a] Fuqiang Huang[a,b]*

Received (in XXX, XXX) Xth XXXXXXXXX 20XX, Accepted Xth XXXXXXXXX 20XX
DOI: 10.1039/b000000x

Black titania nanotube arrays are prepared for the first time, by melted aluminium reduction of pristine anodized and air-annealed titania nanotube arrays. The black titania nanotubes with substantial Ti^{3+} and oxygen vacancies exhibit excellent photoelectrochemical water-splitting performance, due to the improved charge transport and separation and the extended visible light response. An impressive applied bias photon-to-current efficiency of 1.20% is achieved.

Photoelectrochemical (PEC) water-splitting by TiO_2 electrode is regarded as one of the most promising approaches for clean hydrogen production.[1-5] Notably, one dimensional oriented TiO_2 nanotubes (TNTs) prepared by electrochemical anodization have been demonstrated as efficient photoanodes for PEC cell.[6-10] Such a unidirectional architecture decouples the processes of light absorption and charge collection, which can benefit charge separation and transport. Also, TNTs can provide both inner and outer surface for close contact with electrolyte and additional functionalization. However, pristine TNTs suffer from not only low electrical conductivity but also strong surface reflection and weak light harvesting due to the too larger band gap of TiO_2 to utilize visible or infrared light. So the solar-to-hydrogen (STH) conversion efficiency is usually lower than 1%.[11-14] Band engineering of TiO_2 such as dye[15] or quantum dot sensitization,[16] chemical doping[17, 18] and narrow gap semiconductor coupling[19] has been proposed to enhance light absorption and obtain a higher STH efficiency.

Recently, black titania was reported to boost solar light harvesting impressively for enhanced photocatalytic and photoelectrochemical performance.[20-26] The solar absorption of H-doped black titania achieves 83% absorption of the total solar spectrum after nano TiO_2 (commercial P25) was treated by a hydrogen plasma method. The electron concentration of the hydrogenated sample was rather high, up to 7.8×10^{20} cm^{-3}, which can cause local surface plasmon resonance in black titania.[21] As an alternative way to hydrogenation, two-zone melted aluminium (Al) reduction was developed by our group for large-scale production of black TiO_2, which also exhibited high solar absorption (65% of the total solar spectrum) and excellent photocatalytic performance.[22] Black anatase titania thin film prepared by this method possessed a higher electron density (5.61×10^{19} cm^{-3}) compared with untreated film (7.67×10^{17} cm^{-3}). Based on these literature observations, the black titania is suitable to be a promising PEC electrode due to large solar absorption and good electrical conductivity. The black titania nanotube (B-TNT) arrays with a large surface-to-volume ratio can be expected to possess the abilities of strong light capture, good electron transport and high surface area to conduct water-splitting.

Herein, we prepared B-TNT arrays for the first time to the best of our knowledge. We first got as-prepared TNTs (denoted as as-TNTs) via electrochemical anodization, then obtained pristine TNTs (denoted as TNTs) by annealing as-TNTs at 500 °C for 4 h in air, and finally achieved B-TNTs by melted Al reduction treating TNTs at 500 °C for 4 h. The details about Al reduction device and mechanism were clearly described in our previous report.[22] The B-TNTs exhibited high solar absorption covering both ultraviolet and visible light region because of the introduction of a certain amount of Ti^{3+} and oxygen vacancies. They also present an enhanced electron concentration up to 5.55×10^{21} cm^{-3}, much higher than that of TNTs (1.24×10^{19} cm^{-3}). The improved charge transport and charge separation resulted in the much more efficient photoelectrochemical water-splitting. Besides, an enhanced photoelectrochemical response in the visible light region of the B-TNTs was demonstrated. When used as a photoanode for photoelectrochemical cell, an impressive photocurrent of 3.66 mA cm^{-2} and a high applied bias photon-to-current efficiency (ABPE) of 1.20% was achieved under simulated sunlight irradiation, largely surpassing that of TNTs (0.52 mA cm^{-2}, 0.25%).

The absorption spectra of as-TNTs, TNTs and B-TNTs are shown in Figure 1a. The as-TNTs sample presents a typical amorphous titania absorption with an edge at 405 nm, corresponding to a band gap of 3.06 eV. Compared with as-TNTs, a little shift of absorption edge (419 nm) and a slightly enhanced light absorption has taken on the TNTs sample. This red shift of absorption edge is ascribed to the better crystallinity[27] of TNTs after annealing in air. B-TNTs possess a band gap of about 2.65 eV (465 nm), distinctly smaller than as-TNTs and TNTs. Both as-TNTs and TNTs can only respond to UV region, corresponding to the electronic transition from the valence band to the conduction band. However, B-TNTs sample shows a dramatically enhanced light absorption from visible light to near infrared light region, due to the additional transitions between different energy levels of Ti^{3+} states, O vacancies, conduction band and valence band. The generation of Ti^{3+} and oxygen vacancies can be

described by the equation of defect reaction below:

$$2Ti_{Ti}^{\times} + O_{O}^{\times} \rightarrow 2Ti_{Ti}^{'} + 1/2O_2 + V_{O}^{\bullet\bullet}$$

Regardless of other defects, the number of O vacancies is half of Ti^{3+} sites in B-TNTs. The Nis-NIR absorption increases with the the density of Ti^{3+} or O vacancies (Figure S1, Supporting Information), as the density of Ti^{3+} increases with the Al reduction temperature.[22] Inset shows the photograghs of as-TNTs, TNTs and B-TNTs, respectively. The as-TNTs sample is subtransparent with a colour of light yellow, and the TNTs sample displays a yellow color. The B-TNTs sample show a dark black color, in good agreement with the increased visible light absorption.

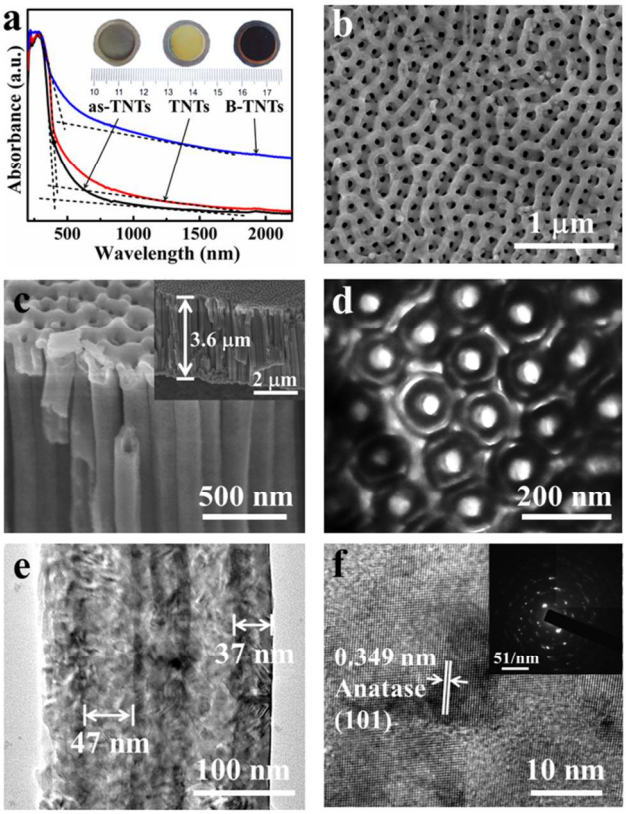

Figure 1. (a) Absorption spectra and photographs (inset) of as-TNTs, TNTs, and B-TNTs. (b) Typical top view FE-SEM of B-TNTs. (c) Side view FE-SEM of B-TNTs, inset is the full side view. (d) Typical top view and (e) side view TEM of B-TNTs. (f) HR-TEM and electron diffraction pattern (inset) of B-TNTS.

Field emission scanning microscopy (FE-SEM) was used to investigate the morphology of B-TNTs. Figure 1b and 1c are the top view and lateral view of the B-TNTs on Ti foil substrate. It is clearly seen that the uniform TiO_2 nanotubes are vertically arranged in order on the surface of Ti foil with an average length of about 3.6 μm. The inner diameter and wall thickness are about 45-55 nm and 35-45 nm, respectively. The morphology and structure of B-TNTs were further examined by TEM, as shown in Figure 1d-1f. From the top view of TEM analysis, B-TNTs consist of nanotubes rather than nanopores. The wall thickness estimated from Figure 1d is approximately 37 nm, and the inner diameter is about 47 nm, in accord with the FE-SEM analysis. According to the EDS spectrum of an area on Figure 1e (Figure S2, Supporting Information), there is no impurity element existing in B-TNTs excluding C and Cu in the carbon-coated copper grid. The selected electron diffraction pattern in the inset of Figure 1f indicates the polycrystalline structure of B-TNTs. The well-resolved lattice fringes of 0.349 nm observed from HR-TEM image (Figure 1f) coincides with the (101) plane of anatase TiO_2 (JCPDF No. 21-1272), demonstrating the anatase phase of B-TNTs.

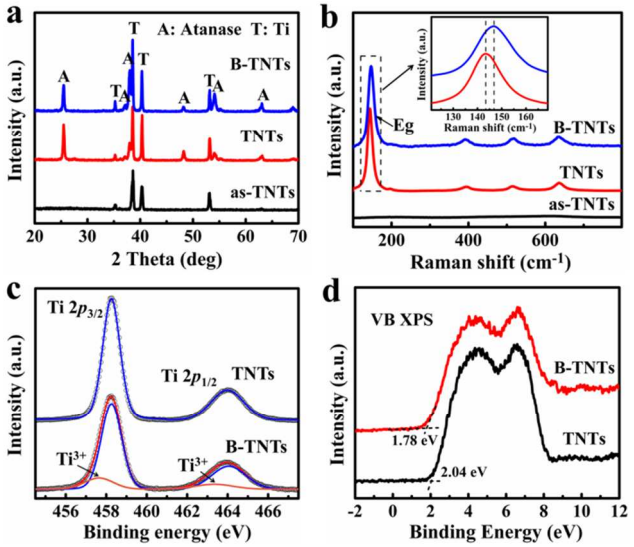

Figure 2. (a) XRD patterns and (b) Raman spectra of TNTs with different annealing treatment, inset is the magnification of E_g peak. (c) Ti 2*p* XPS spectra of TNTs and B-TNTs. Black circles are the experimental data, which can be decomposed into a superposition of two fitting curves of Ti^{4+} (shown in blue) and Ti^{3+} (shown in orange). The red curve is the summation of the two decomposed curves. (d) XPS valence band spectra of TNTs and B-TNTs.

XRD patterns dictating the phase evolution with different annealing processes are shown in Figure 2a. Only the peaks of Ti substrate are observed for as-TNTs, verifying their amorphous feature. For pattern of TNTs, additional characteristic peaks of anatase TiO_2 emerge and no other phase of TiO_2 like rutile is found. As with TNTs, the B-TNTs sample comprises the same two phases, judged from its XRD pattern. The peak positions of B-TNTs are almost unchanged, compared with the corresponding peaks of TNTs, indicating the identical interplanar distances of anatase TiO_2 in TNTs and B-TNTs. However, there is a noticeable change in the intensity ratios of different peaks, which may be caused by the crystal orientation growth during the Al reduction process.

The change of chemical coordination structure of titania tubes is unambiguously supported by Raman spectroscopy (Figure 2b). Four characteristic Raman peaks at 143.4, 395.0, 515.3 and 636.1 cm^{-1} in TNTs are assigned to the E_g, B_{1g}, A_{1g} or B_{2g} and E_g mode of anatase phase, respectively.[28] It is obvious that the frequency of the strongest *Eg* mode in B-TNTs, which arises from the external vibration of Ti–O bond, has a blue shift to 146.7 cm^{-1} as well as a broadened full width of half maximum (FWHM) relative to TNTs. This can be attributed to the increased amount of oxygen vacancies in B-TNTs.[22, 29] None of the peaks appear in the spectrum of as-TNTs, confirming their amorphous structure

again.

XPS was performed to investigate the change of surface bonding and electronic valence band position of B-TNTs induced by Al reduction treatment. The Ti $2p_{3/2}$ and $2p_{1/2}$ XPS peaks in TNTs are centered at binding energies of 458.3 and 464.0 eV, as shown in Figure 2c, which is typical for the Ti^{4+}–O bonds in TiO_2.[20] Compared with TNTs, additional small peaks centering separately at 457.7 eV and 463.3 eV in B-TNTs conform to the $2p_{3/2}$ and $2p_{1/2}$ peaks of Ti^{3+}.[30-32] The emerging Ti^{3+} signals suggest that oxygen vacancies are introduced into B-TNTs during the Al reduction process. The O 1*s* XPS spectra of B-TNTs and TNTs are almost the same (Figure S3, Supporting Information), with a single peak at 529.6 eV assigned to Ti–O bonds. Both Raman and XPS analyses indicate the generation of oxygen vacancies in B-TNTs, which can serve as donors to increase the electron concentration of anatase TiO_2.[33, 34] The valence band spectra of TNTs and B-TNTs are shown in Figure 2d. The valence band maxima are estimated by linear extrapolation of the peaks to the baselines, which derives a band edge position of 2.04 eV for TNTs and 1.78 eV for B-TNTs below the Fermi energy. This result confirms Al reduction treatment has driven an upward shift effect on the valence band position at the TNTs surface, which may be due to that the disorders and defects induced by Al reduction generate some localized states above the valence band edge.[25] Given the blue shift of valence maximum, a narrowed band-gap would occur in B-TNTs. However, the change of the band-gap is insufficient to result in such an overall absorption in the visible and near infrared range. Besides, the band gap narrowing for B-TNTs due to Ti^{3+} acceptor states can hardly be measured. Based on previous report,[22] they could generate a tail of conduction band about 0.7 eV below the conduction band maximum of TiO_2. The dark color of B-TNTs can be derived from the formation of impurity/defect states in the band gap of B-TNTs during Al reduction treatment. The full XPS spectrum also confirmed that the B-TNTs sample is not doped with other elements (Figure S4, Supporting Information), so the defect states are attributed to the formation of oxygen vacancies.

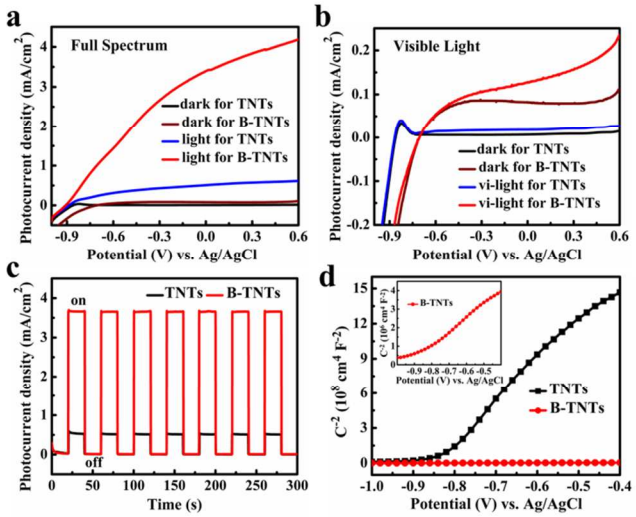

Figure 3. (a) Linear sweep voltammograms collected under 100 mW cm^{-2} illumination using three electrodes setup (TNTs or B-TNTs working, Pt counter, Ag/AgCl reference electrode, scan rate of 50 mV/s) in 1 M NaOH electrolyte (pH = 13.6). (b) Linear sweep voltammograms collected under visible light, the UV light was eliminated by a 420 nm cutoff glass light filter. (c) Transient photocurrent responses of TNTs and B-TNTs at 0.23 V vs. Ag/AgCl. (d) Mott-Schottky plots collected at a frequency of 1 kHz in dark.

To investigate the photoelectrochemical properties of B-TNTs, a set of linear sweeps were recorded in dark and under 100 mW cm^{-2} illumination, as shown in Figure 3a. The potential was swept linearly at a scan rate of 50 mV/s between −1.0 and 0.6 V vs. Ag/AgCl in 1 M NaOH electrolyte (pH = 13.6). Both photoelectrodes show very low dark current with respect to their respective photocurrent, indicating that no drastic electrocatalytic water splitting occurs. Obviously, the photocurrent of B-TNTs under illumination is distinctly higher than that of TNTs. Furthermore, the onset potential of photocurrent reveals a slight shift from −0.887 $V_{Ag/AgCl}$ for pristine TNTs to −0.909 $V_{Ag/AgCl}$ for B-TNTs. The higher photocurrent density and lower onset potential demonstrate more efficient charge separation and transport in the B-TNTs, compared with TNTs. It is worth noting that the photocurrent under visible light ($\lambda \geq 420$ nm) of B-TNTs is also obviously higher than that of TNTs, and the dark current for B-TNTs turns significant relative to the photocurrent. The greatly enhanced electrical conductivity of B-TNTs due to the increased carrier density, coupled with the massive defect states in B-TNTs, accounts for the distinct increase of dark current. For pristine TNTs, the negative current below -0.9 V and the peak in the current at near -0.85 V for both the dark scan and the visible light scan may be due to the intercalation of Na^+ ions into TiO_2 nanotubes followed by its deintercalation at higher potential.[35] For B-TNTs, the peak becomes broad and indistinct due to the greater balanced current at the subsequent higher potential. Subtracting their respective dark current, the actual photocurrent induced by visible light of B-TNTs (0.065 mA cm^{-2}) at 0.23 $V_{Ag/AgCl}$, is about five times larger than that of TNTs (0.012 mA cm^{-2}). This enhancement should be attributed to the enhanced visible light absorption of B-TNTs which is mainly caused by the increased amount of oxygen vacancy donor sites, and contribute to the overall photoelectrochemical performance of B-TNTs more or less. To investigate the photoresponses of TNTs and B-TNTs, the photoelectrochemical measurement was carried out under illumination with several 40 s light on/off cycles at 0.23 $V_{Ag/AgCl}$. The plots of the transient photocurrent responses vs. time are shown in Figure 3c. Both samples have good photoresponses in chopped light cycles. Without illumination, the current values are almost zero while the photocurrent rapidly rises to a steady-state value upon illumination, which is reproducible for several on/off cycles with almost the identical photocurrent and dark current. The observed steady-state photocurrent of B-TNTs (3.66 mA cm^{-2}) is nearly seven times higher than that of TNTs (0.52 mA cm^{-2}), indicating the larger amount of photo-induced carriers in B-TNTs owing to the improved charge separation and their more efficient transport process from the wall of B-TNTs to the Ti foil substrate. The transient photocurrent responses to visible light of TNTs and B-TNTs are also measured (Figure S5, Supporting Information).

Electrochemical impedance measurements were conducted on TNTs and B-TNTs. Mott-Schottky plots of both samples show a positive slope (Figure 3d), characteristic of n-type semiconductor. The huge difference of slopes of the two plots indicates a spectacular disparity of donor densities in TNTs and B-TNTs.

Carrier density is calculated from the slope using the following equation:

$$N_d = (2/e_0\varepsilon\varepsilon_0)\,[\mathrm{d}(1/C^2)/\mathrm{d}V]^{-1},$$

where e_0, ε, ε_0, N_d and $\mathrm{d}(1/C^2)/\mathrm{d}V$ represent the electron charge, the dielectric constant of TiO_2 (31 for anatase),[36] the permittivity of vacuum, the donor density and the straight slope, respectively. The calculated electron densities of TNTs and B-TNTs are 1.24×10^{19} and 5.55×10^{21} cm^{-3} separately. This indicates that the Al reduction process induces an exponential increase of electron density, due to the introduction of substantial oxygen vacancies. In fact, Al reduction can be considered as such a process that melted Al reductant loses electrons and Ti^{4+} ions accept them on the basis of the law of electron conservation, with the appended oxygen ions transferring to Al_2O_3 from TiO_2. Thus the donor density and electrical conductivity of B-TNTs could be greatly enhanced. Meanwhile, the expected upward shift of Fermi level caused by the increased electron density can lead a significantly larger degree of band bending at the surface of B-TNTs, which could promote the charge separation at the interface of B-TNTs and electrolyte.[23, 37] Therefore, the improved charge transport, along with the facilitated charge separation, is responsible for the much more efficient photoelectrochemical water-splitting. We have reasons to believe that better photoelectrochemical performance of B-TNTs could be achieved by optimizing the morphology and structure of anodized TiO_2 nanotubes and the parameters of Al reduction process.

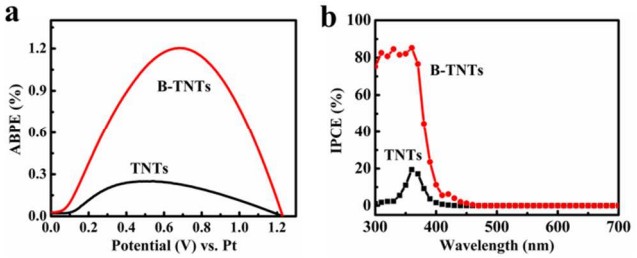

Figure 4. (a) ABPE of TNTs and B-TNTs as a function of applied potential. (b) IPCE spectra in the region of 300-700 nm at 0.23 V vs. Ag/AgCl.

Applied bias photon-to-current efficiency (ABPE) is an important figure of merit to measure the PEC water-splitting performance of a semiconductor photoanode, which can represent the STH efficiency more or less. The 2-electrode measurement under the same conditions as 3-electrode test was conducted to obtain 2-electrode *J-V* curves for the ABPE calculation. The ABPE of photoanode can be calculated using the equation:[38]

$$\mathrm{ABPE}\ (\%) = I\,(1.23 - V_{bias})/J_{light},$$

where V_{bias} is the applied bias between working electrode and counter electrode, I is photocurrent density at the measured bias, and J_{light} is the irradiance intensity of 100 mW cm^{-2}. The 2-electrode photocurrent-potential curves The ABPE calculated from the *J-V* curves (Figure S6, Supporting Information) plotted as a function of the applied bias are shown in Figure 4a. The TNTs photoanode shows a maximum conversion efficiency of 0.25% at 0.49 V (vs. Pt), while the B-TNTs sample achieves an impressive efficiency of 1.20% at a higher bias of 0.68 V (vs. Pt).

In order to understand the interplay between the photoactivity and the light absorption of two types of titania nanotubes, incident-photon-to-current-conversion efficiency (IPCE) measurements were performed on TNTs and B-TNTs photoanodes at 0.23 $V_{Ag/AgCl}$ (Figure 4b). The IPCE can be expressed by the equation:[39]

$$\mathrm{IPCE} = (1240\,I)/(\lambda J_{light}),$$

where I is the measured photocurrent density at a specific wavelength, λ is the wavelength of incident light, and J_{light} is the measured irradiance at a specific wavelength. In comparison with TNTs, the B-TNTs sample exhibits greatly enhanced photoactivity over the entire UV region and reaches the IPCE values around 80% in the wavelength range from 300 to 370 nm. It indicates that the UV light is effectively used for PEC water splitting by B-TNTs, in which the separation and transport of photoexcited charge carriers are more efficient. Moreover, the IPCE value is also larger in the visible light region from 400 nm to 460 nm for the B-TNTs, in agreement with the extended absorption in the absorption spectrum (Figure 1a) and the increased photocurrent under visible light (Figure 3b). It indicates that not only highly improved efficiency of photoelectrochemical conversion under UV light can be acquired from B-TNTs, but also the expanded photoresponse range to visible light.

In summary, black TiO_2 nanotube arrays have been successfully prepared by Al reduction method and used as photoanode of photoelectrochemical cell for water-splitting. A considerable amount of Ti^{3+} and oxygen vacancies were introduced into B-TNTs, resulting in a great improvement of carrier density. Moreover, the photoelectrochemical response region of B-TNTs was demonstrated to expand to visible light. The improved charge transport and charge separation, together with the additional visible light photoresponse, resulted in the much more efficient photoelectrochemical water-splitting. The B-TNTs photoanode exhibited a large photocurrent of 3.65 mA cm^{-2} and a high ABPE of 1.20%, which was about 5 times higher than that of TNTs and hopeful to be further improved via our future optimization effort.

Acknowledgements

This work is supported by NSF of China (Grant Nos. 51125006, 91122034, 51121064), 863 Programs of China (Grant No. 2011AA050505), CAS program (Grant Nos. KJCX2-EW-W11, KGZD-EW-303), and STC of Shanghai (Grant No.13JC1405700).

Notes and references

[a] *State Key Laboratory of High Performance Ceramics and Superfine Microstructure and CAS Key Laboratory of Materials for Energy Conversion, Shanghai Institute of Ceramics, Chinese Academy of Sciences, Shanghai 200050, P.R. China. E-mail: huangfq@mail.sic.ac.cn*
[b] *Beijing National Laboratory for Molecular Sciences and State Key Laboratory of Rare Earth Materials Chemistry and Applications, College of Chemistry and Molecular Engineering, Peking University, Beijing 100871, P.R. China*

† Electronic Supplementary Information (ESI) available: [Experimental details, EDS spectrum, O 1*s* XPS spectra, XPS survey spectra, transient photocurrent response to visible light]. See DOI: 10.1039/b000000x/

1 A. Fujishima and K. Honda, *Nature*, 1972, **238**, 37.

2 M. R. Hoffmann, S. T. Martin, W. Y. Choi and D. W. Bahnemann, *Chem. Rev.*, 1995, **95**, 69.
3 M. Gratzel, *Nature*, 2001, **414**, 338.
4 S. U. M. Khan, M. Al-Shahry and W. B. Ingler, *Science*, 2002, **297**, 2243.
5 K. Shankar, J. I. Basham, N. K. Allam, O. K. Varghese, G. K. Mor, X. J. Feng, M. Paulose, J. A. Seabold, K. S. Choi and C. A. Grimes, *J. Phys. Chem. C*, 2009, **113**, 6327.
6 G. K. Mor, K. Shankar, O. K. Varghese and C. A. Grimes, *J. Mater. Res.*, 2004, **19**, 2989.
7 G. K. Mor, K. Shankar, M. Paulose, O. K. Varghese and C. A. Grimes, *Nano. Lett.*, 2005, **5**, 191.
8 Y. B. Liu, J. H. Li, B. X. Zhou, J. Bai, Q. Zheng, J. L. Zhang and W. M. Cai, *Environ. Chem. Lett.*, 2009, **7**, 363.
9 Z. H. Zhang, M. F. Hossain and T. Takahashi, *Int. J. Hydrogen Energ.*, 2010, **35**, 8528.
10 Y. Sun, K. P. Yan, G. X. Wang, W. Guo and T. L. Ma, *J. Phys. Chem. C*, 2011, **115**, 12844.
11 J. H. Park, O. O. Park and S. Kim, *Appl. Phys. Lett.*, 2006, **89**, 163106.
12 N. K. Allam, K. Shankar and C. A. Grimes, *J. Mater. Chem.*, 2008, **18**, 2341.
13 N. K. Allam and C. A. Grimes, *Langmuir*, 2009, **25**, 7234.
14 Z. H. Zhang, L. B. Zhang, M. N. Hedhili, H. N. Zhang and P. Wang, *Nano. Lett.*, 2013, **13**, 14.
15 W. J. Youngblood, S. H. A. Lee, Y. Kobayashi, E. A. Hernandez-Pagan, P. G. Hoertz, T. A. Moore, A. L. Moore, D. Gust and T. E. Mallouk, *J. Am. Chem. Soc.*, 2009, **131**, 926.
16 X. F. Gao, H. B. Li, W. T. Sun, Q. Chen, F. Q. Tang and L. M. Peng, *J. Phys. Chem. C.*, 2009, **113**, 7531.
17 J. H. Park, S. Kim and A. J. Bard, *Nano. Lett.*, 2006, **6**, 24.
18 S. Hoang, S. P. Berglund, N. T. Hahn, A. J. Bard and C. B. Mullins, *J. Am. Chem. Soc.*, 2012, **134**, 3659.
19 Y. X. Yin, Z. G. Jin and F. Hou, *Nanotechnology*, 2007, **18**.
20 X. B. Chen, L. Liu, P. Y. Yu and S. S. Mao, *Science*, 2011, **331**, 746.
21 Z. Wang, C. Y. Yang, T. Q. Lin, H. Yin, P. Chen, D. Y. Wan, F. F. Xu, F. Q. Huang, J. H. Lin, X. M. Xie and M. H. Jiang, *Adv. Funct. Mater.*, 2013, **23**, 5444.
22 Z. Wang, C. Y. Yang, T. Q. Lin, H. Yin, P. Chen, D. Y. Wan, F. F. Xu, F. Q. Huang, J. H. Lin, X. M. Xie and M. H. Jiang, *Energ. Environ. Sci.*, 2013, **6**, 3007.
23 C. Yang, Z. Wang, T. Lin, H. Yin, X. Lu, D. Wan, T. Xu, C. Zheng, J. Lin, F. Huang, X. Xie and M. Jiang, *J. Am. Chem. Soc.*, 2013, **135**, 17831.
24 H. Yin, T. Q. Lin, C. Y. Yang, Z. Wang, G. L. Zhu, T. Xu, X. M. Xie, F. Q. Huang and M. H. Jiang, *Chem.-Eur. J.*, 2013, **19**, 13313.
25 G. L. Zhu, T. Q. Lin, X. J. Lu, W. Zhao, C. Y. Yang, Z. Wang, H. Yin, Z. Q. Liu, F. Q. Huang and J. H. Lin, *J. Mater. Chem. A*, 2013, **1**, 9650.
26 T. Lin, C. Yang, Z. Wang, H. Yin, X. Lu, F. Huang, J. Lin, X. Xie and M. Jiang, *Energ. Environ. Sci.*, 2014, DOI: 10.1039/C3EE42708K.
27 Y. Gao, Y. Masuda, Z. Peng, T. Yonezawa and K. Koumoto, *J. Mater. Chem.*, 2003, **13**, 608.
28 C. Xu, P. Zhang and L. Yan, *J. Raman Spectrosc.*, 2001, **32**, 862.
29 A. Li Bassi, D. Cattaneo, V. Russo, C. Bottani, E. Barborini, T. Mazza, P. Piseri, P. Milani, F. Ernst and K. Wegner, *J. Appl. Phys.*, 2005, **98**, 074305.
30 X. D. Jiang, Y. P. Zhang, J. Jiang, Y. S. Rong, Y. C. Wang, Y. C. Wu and C. X. Pan, *J. Phys. Chem. C*, 2012, **116**, 22619.
31 M. M. Rahman, K. M. Krishna, T. Soga, T. Jimbo and M. Umeno, *J. Phys. Chem. Solids*, 1999, **60**, 201.
32 L. B. Xiong, J. L. Li, B. Yang and Y. Yu, *J. Nanomater.*, 2012, DOI: 10.1155/2012/831524.
33 G. Mattioli, F. Filippone, P. Alippi and A. A. Bonapasta, *Phys. Rev. B*, 2008, **78**, 241201.
34 S. Na-Phattalung, M. F. Smith, K. Kim, M.-H. Du, S.-H. Wei, S. Zhang and S. Limpijumnong, *Phys. Rev. B*, 2006, **73**, 125205.
35 W. Smith, A. Wolcott, R. C. Fitzmorris, J. Z. Zhang and Y. Zhao, *J. Mater. Chem.*, 2011, **21**, 10792.
36 H. Tang, K. Prasad, R. Sanjines, P. Schmid and F. Levy, *J. Appl. Phys.*, 1994, **75**, 2042.
37 G. Wang, H. Wang, Y. Ling, Y. Tang, X. Yang, R. C. Fitzmorris, C. Wang, J. Z. Zhang and Y. Li, *Nano. Lett.*, 2011, **11**, 3026.
38 T. W. Kim and K.-S. Choi, *Science*, 2014, **343**, 990.
39 M. G. Walter, E. L. Warren, J. R. McKone, S. W. Boettcher, Q. Mi, E. A. Santori and N. S. Lewis, *Chem. Rev.*, 2010, **110**, 6446.